

Journal of Design Against Fatigue

https://minerva-aset.com/jdaf/

MINERVA ASET

A predictive approach for thermal fatigue crack growth behaviour of shot peened Ni75 alloy

B. Salehnasab [a*], J. Marzbanrad [a], E. Poursaeidi [b]

[a] *School of Automotive Engineering, Iran University of Science and Technology, Narmak, Tehran, Iran*
[b] *Mechanical Engineering Department, Faculty of Engineering, University of Zanjan, Iran*

P A P E R I N F O

Paper history:
Received 11 March 2023
Received in revised form 26 March 2023
Accepted 28 March 2023

Keywords:
Shot peening treatment
Thermal fatigue
Crack propagation
Fatigue life model
Residual stress

A B S T R A C T

This study presents an approach to predict the effects of shot peening on the thermal fatigue crack propagation behaviour of nickel-based Ni75 alloy. For this purpose, from an engineering perspective, comprising experimental tests data and finite element simulations, were used to estimate the thermal fatigue crack propagation behaviour of the material. Despite many other studies that have been performed to evaluate the fatigue crack growth behavior, only a few were previously conducted on thermal fatigue damage in different types of materials. Furthermore, the interaction of shot peening treatment and thermal fatigue crack propagation behavior is rare. Comparison of the results from the experimental test and FE model showed that the model appropriately predicted the thermal fatigue crack growth behaviour. The fracture mechanism evaluation showed that the compressive residual stress, induced by shot peening treatment, reduced both the crack opening and secondary crack branching. Also, the results show the crack initiation life of the shot peened specimen (SP) is about 2.5 times more than the non shotpeened specimen (NSP). Moreover, the microscopy analysis showed that the failure mechanism of the NSP and SP specimens were transgranular and a combination of intergranular and transgranular cracking, respectively.

doi:

1. INTRODUCTION

Temperature fluctuation can introduce transient stresses that unavoidably cause thermal fatigue damage by irregular cyclic expansion and shrinkage [1]. Thermal fatigue damage involves two steps; first, the crack initiation, and second, propagation of cracks [2-4]. When some cracks are initiated, the primary cracks are susceptible to growth by thermal stresses arising from the temperature gradients cycles. Eventually, the component fails after a critical number of cycles that is defined as fatigue life which includes initiation and propagation periods [5, 6]. Therefore, the prediction of crack growth behaviour during thermal cycles can help engineers to predict the lifetime of a component accurately by considering the operational loading conditions [4]. In many industrial applications, especially in the energy sector, there are components which operate at high temperatures and under cyclic loading conditions, hence an improvement in understanding of the thermal fatigue crack growth behaviour will help to enhance the life assessment of such engineering component.

Some studies were previously conducted on the thermal fatigue damage in different types of materials, especially Ni-based superalloys. Meyer-Olbersleben et al. [7] investigated the thermal fatigue behaviour of the combustor alloys IN617 and HAYNES 230 before and after welding. Poursaeidi et al. [8] investigated the effects of emergency and fired shut down on transient thermal fatigue life of a gas turbine casing by considering linear elastic and elastic-perfectly plastic material behaviour. Poursaeidi et al. [9] investigated the thermal fatigue crack growth prediction in a heavy-duty gas turbine casing. Kamouri Yousefabad et al. [10] investigated the effect of non-uniform combustion temperature profile on thermal fatigue crack initiation

*Corresponding Author Email: b_salehnasab@auto.iust.ac.ir (Behnam Salehnasab))

Please cite this article as: B. Salehnasab, J. Marzbanrad, E. Poursaeidi, A predictive approach for thermal fatigue crack growth behaviour of shot peened Ni75 alloy, ***Journal of Design Against Fatigue,*** Vol. 1, No. 1, (2023), 1-14

of an air-cooled gas turbine nozzle. Zhang et al. [1] investigated the crack initiation and propagation mechanisms during thermal fatigue in directionally solidified superalloy DZ125. Bombač et al. [11] investigated the thermal fatigue behaviour of roller steel at high temperatures. Li et al. [12] investigated crack initiation and growth around holes of Ni-based single crystal superalloy during thermal fatigue. Vetriselvan et al. [13] experimentally and numerically investigated the thermal fatigue behaviour of 9Cr1Mo steel tubes. Liu et al. [14] investigated the thermal fatigue evaluation of AISI H13 steel surface modified by gas nitriding with pre-and post-shot peening. Qayyum et al. [15] performed numerical simulations to explore the thermal fatigue behaviour in a cracked disc of AISI H-11 tool steel. Pei et al. [16] studied transient thermal fatigue crack propagation behaviour of a nickel-based single-crystal superalloy. Pei et al. [17] investigated the crack initiation behaviour of a Ni-based single crystal superalloy under transient thermal stress. Bazvandi and Poursaeidi [18] examined the improvement of transient thermal fatigue crack propagation life of gas turbines casings through the application of additional holes. Banaszkiewicz [19] explored crack initiation in impulse steam turbine rotors subject to thermo-mechanical fatigue by using numerical methods. Getsov et al. [20] investigated thermal fatigue analysis of turbine discs by using thermo-elasto-visco-plastic material model and deformation failure criterion. Mazlan et al. [21] investigated experimental and numerical analysis of fatigue life of aluminum Al 2024-T351 at elevated temperature .

For the effect of shot peening treatment on fatigue crack propagation in metal alloys some studies were carried out. Qin et al. [22] investigated effects of shot peening with different coverage on surface integrity and fatigue crack growth properties of 7B50-T7751 aluminum alloy. Wang et al. [23] investigated fatigue crack propagation in a residual stress field induced by shot peening. Wang et al. [24] investigated effect of shot peening on fatigue crack propagation of Ti6Al4V. He et al. [25] investigated fatigue crack growth behaviour in the LCF regime in a shot peened steam turbine blade material. Ferreira et al. [26] investigated effects of shot peening and stress ratio on the fatigue crack propagation of AL 7475-T7351 specimens. Li et al. [27] investigated prediction of fatigue crack propagation behavior of AA2524 after laser shot peening .

In order to evaluate the thermal fatigue behaviour of engineering materials, different researchers have developed specific experimental test setups, such as a disc heated by induction coil [28], the hot dropping of cylinders in molten aluminum [29], halogen lamps heating [30], electrical heating followed by water splashing [31], laser heating [32], furnace heating with water quenching [33], and convection/combustion heating [34]. Luo et al. [35] investigated the effect of laser shock peening, shot peening and their combination on the microstructure and fatigue properties of Ti-6Al-4V titanium alloy.

This study aims to present an approach based on a combination of experimental tests data obtained from the thermal fatigue test set-up developed in this work and finite element (FE) simulation results to predict the thermal fatigue crack propagation behaviour of shot peened Ni75 alloy. The developed model in the present study is based on the coupled thermal-displacement problem theory and the Paris law. For this purpose, a set of experiments and FE simulations were carried out to predict the crack growth behaviour of centre-hole specimens made of a Ni-based alloy under thermal cyclic loading conditions. Also, to evaluate the fracture mechanisms of the material with and without residual stress, optical and scanning electron microscopy were conducted.

2. MATERIAL AND METHODS

2. 1. MATERIAL AND SAMPLE PREPARATION

The material used in this research is Ni75 alloy which is typically used for heavy duty gas turbine engine applications. The chemical composition of the material is presented in **TABLE 1** [36]. Ni75 is a uniform solid-solution of Ni–20Cr with inter-granularly occurring primary carbides of general form MC as well as chromium-rich grain boundary carbides of type M23C6 [36]. The material examined in this study was hot-rolled and solution heat-treated for 10 minutes at 1050°C followed by air cooling. The mechanical properties and the microstructure of the Ni75 material are shown in **Figure 1** and **2**, respectively [37]. As seen in **Figure 1**, the yield stress, elastic Young's modulus and coefficient of thermal expansion were characterised for a wide range of temperatures from 25°C to 1000°C. The samples used for microstructural analysis were electro etched in a solution of 36 ml HNO_3, 35 ml H_2SO_4, and 9.5 ml H_3PO_4 reagent at the voltage of 7 V for 120 s. According to **Figure 2**, fine metal grains are observed in the material microstructure. The mean grain size of Ni75 alloy used in this study was found to be 12 μm with a mean grain area of 125 μm2, measured following the guidelines provided in ASTM E-112. The hardness values found from indentation tests performed on the examined material were 40–42 HRC. Subsequent to material characterisation tests, six thermal fatigue test specimens containing a centre hole-edge crack were extracted from a Ni75 sheet of 3 mm thick using the electrical discharge machining (EDM) technique. **Figure 3** shows the specimen geometry.

Table 1. Chemical composition of Ni75 alloy (wt%)

Ni	C	Cr	Cu	Fe	Mn	Si	Ti
Base	0.052	19.91	0.038	0.47	0.013	0.32	2.44
Mo	**V**	**Al**	**Mg**	**Nb**	**W**		
0.21	0.026	1.01	0.024	0.05	0.024		

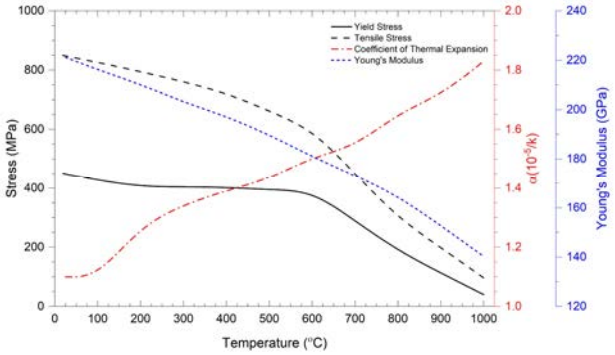


Figure 1. The physical and mechanical properties of Ni75 alloy

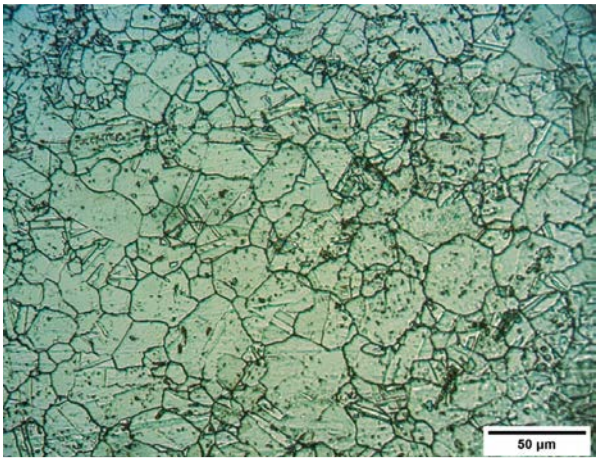


Figure 2. Optical micrograph of the microstructure of Ni75 alloy

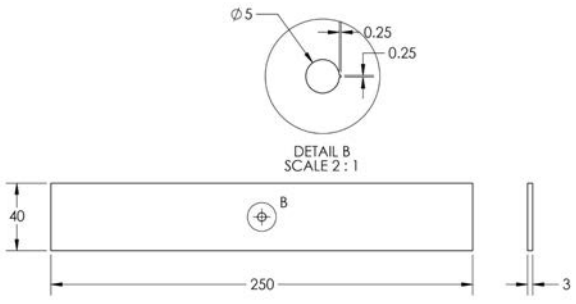


Figure 3. Schematic drawing of the thermal fatigue test specimen (in mm)

2.2. SHOT PEENING PROCESS

Out of six thermal fatigue test specimens, three specimens were shot peened according to the SAE AMS2430 standard [38] with a 18A Almen intensity and surface coverage of 100%. The shot peening process was performed by using a pneumatic shot peening machine. The peening balls were made from SAE J2175 and the diameter and hardness of the balls were 0.4 to 0.6 mm and 55–60 Rockwell C, respectively. The surface roughness, R_a, of the specimens with and without shot peening was measured using a portable Mitutoyo Surftest SJ-210 machine. **Figure 4** shows the surface roughness of shot peened (SP) and non-shot peened (NSP) specimens. The R_a value of each test condition (i.e. NSP and SP) is an average value across three specimens of the same condition. As seen in **Figure 4**, the mean value of surface roughness of SP specimens is about 11 times more than that of NSP specimens, and plastic deformations are clearly seen on the SP specimen's surface.

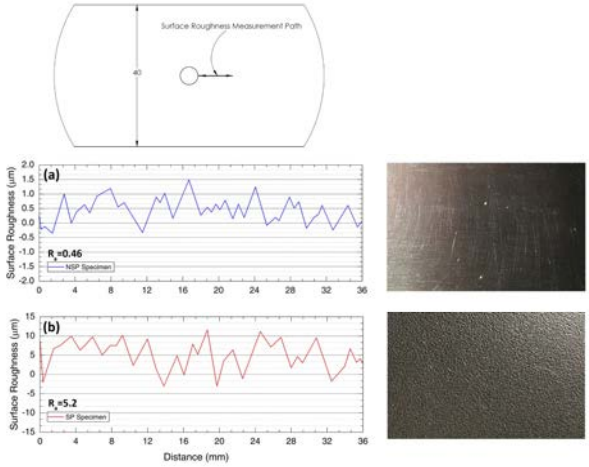


Figure 4. The surface roughness of the specimens: (a) NSP specimen; and (b) SP specimen

2.3. RESIDUAL STRESS MEASUREMENT

The X-Ray Diffraction method (XRD) was used to measure the residual stresses induced by the shot peening process along the transverse direction. The penetration depth of the X-ray beam in the Ni75 alloy is about 10 µm; therefore, the Electrochemical Machining (ECM) was used to remove the layers to obtain a full residual stress profile in the thickness of the specimen. The depth of each layer was precisely measured by a micrometer, with a resolution of 0.01 mm. Cu-Kα radiation at 40 kV, 30 mA, and 1°/min and a beam spot size of about 1×1 mm2 were used. **Figure 5** shows the residual stresses induced by the shot peening process versus the specimen depth. Maximum compressive residual stresses are obtained in near-surface points, as expected, and by increasing the depth of the specimens the induced residual stress is decreased significantly.

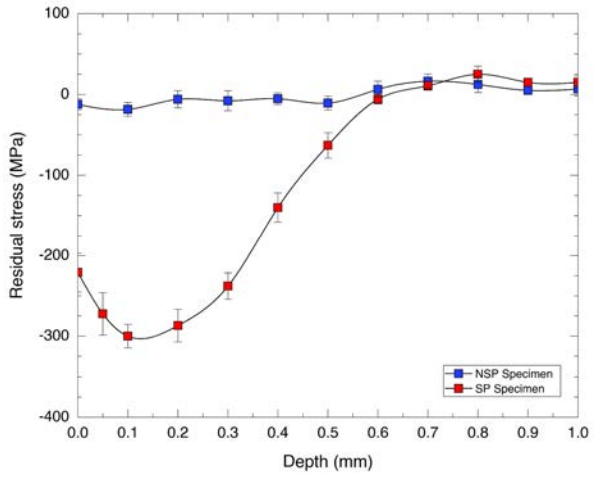


Figure 5. XRD residual stress measurement on the NSP and SP thermal fatigue test specimens

2.4. THERMAL FATIGUE TEST SETUP

In the present study, the thermal fatigue tests were performed by a home-made and calibrated test set-up which includes a coil and fan system to apply the thermal cyclic loading condition on a test specimen. The experimental set-up of the thermal fatigue tests conducted in this study is shown in **Figure 6(a)** and **(b)**. The tests were performed on the NSP and SP specimens containing a hole-edge crack. Each specimen was subjected to three thermal loading conditions. The thermal loading cycle included a transient temperature increase up from room temperature to 700 °C, a steady-state condition at the temperature of 700 °C, and a transient temperature decrease to room temperature. **Figure 6(c)** shows the thermal loading cycle that was applied to the test specimens. All the thermal fatigue tests were carried out at a zero-loading ratio (R = 0) and the test method is referred to "HB 6660-1992 test method for thermal fatigue of sheet metal. In this study, the thermal fatigue tests were conducted on three nominally identical specimens for each of the NSP and SP conditions and the average parameters such as the main crack length of three specimens obtained by the test were used in the analysis. The specimens were heated up by a coil to a constant temperature of 700 °C and after that, they were cooled down by air blown through the blower. Thermocouples were welded on the specimens' outer surface and used to continuously monitor the temperature throughout the tests. The heating coil covered approximately 80 mm of the middle part of the specimen. The temperature acquisition frequency was 3Hz and a temperature control system, controlled the fluctuation that did not exceed ±5°C and it was used to control the heat-up and cool-down process by using a coil and fan. A digital counter was used for recording the cycle counting. During the thermal fatigue tests, the specimens were inspected every 200 cycles for the NSP samples and every 500 cycles for the SP samples to detect and measure the crack length. A Dino-lite digital microscope to detect the crack during the test and the commercial image processing software to calculate the crack length were used. The thermal fatigue tests on the NSP and SP specimens were continued until the sample failed or the crack reached a certain length.

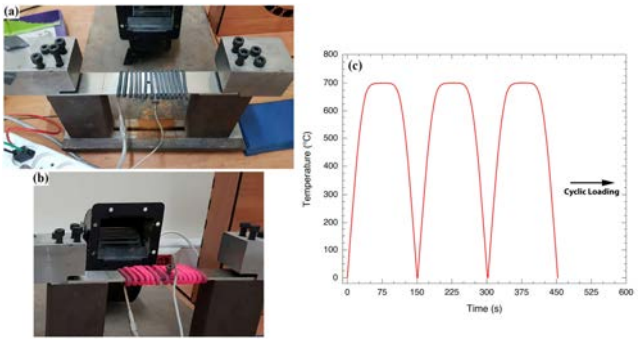


Figure 6. Experimental set-up for thermal fatigue tests (a) before heat up, (b) after heat up, (c) Applied thermal cyclic loading pattern

3. NUMERICAL MODELLING FRAMEWORK

3.1. FATIGUE CRACK GROWTH FORMULATION

In this section, the numerical modelling procedure for crack propagation prediction is described. In the first step, the transient heat conduction for a three dimensional (3D) anisotropic material is formulated by:

$$\frac{\partial^2 T}{\partial x^2}+\frac{\partial^2 T}{\partial y^2}+\frac{\partial^2 T}{\partial z^2}=\frac{\rho C\,\partial T}{\lambda \partial T} \quad (1)$$

where T is the thermal loading condition, C is the specific heat, λ is the thermal conductivity, ρ is the density, and t is the time. The Paris law was employed to simulate the fatigue crack growth rate, da/dN, by using the equivalent stress intensity factor (SIF) range. The J-integral is generally used in rate-dependent quasi-static fracture analysis to describe the energy release associated with crack growth [39]. The energy release rate is obtained by:

$$J=\oint_{\Gamma}\left[Wdy-\sigma_{ij}\eta_j\frac{\partial u_i}{\partial x}ds\right] \quad (2)$$

where Γ is a contour around the crack tip starting from the lower crack surface to the upper crack surface in a counter-clockwise path and dΓ stands for the length

increment along the contour Γ. For a linear-elastic material, W is the elastic strain energy, η is a unit matrix, σ is the stress matrix and ∂u/∂x is the strain matrix. The standard path-independent definition of the J-integral may change to a path-dependent form when the residual stresses are remarkable; thus, the J-integral evaluation must include an additional term of the residual stress field [40]. To consider the residual stress effect on the J-integral, a correction method was developed [41]. Based on the correction method, in the presence of the initial strain, the total strain is divided into two separate terms.

$$\varepsilon_{ij} = \varepsilon_{ij}^{0} + \varepsilon_{ij}^{m} \quad (3)$$

Where ε_{ij} is total strain, ε_{ij}^{0} is initial strain, and ε_{ij}^{m} is the strain caused by mechanical loading. Work density definition is changed by the modification. The modified work density is redefined to withdraw the initial plastic dissipation accumulated during the processes producing the initial state from the total work density. Finally, Equation (2) is written as:

$$J = \int_{\Gamma}\left[Wdy - \sigma_{ij}\eta_{j}\frac{\partial u_{i}}{\partial x}ds \right] + \int_{A}\sigma_{ij}\frac{\partial \varepsilon_{ij}^{0}}{\partial x}dA \quad (4)$$

where W is defined by:

$$W = \int_{0}^{\varepsilon_{ij}^{m}} \sigma_{ij} d\varepsilon_{ij}^{m} \quad (5)$$

Under elastic deformation conditions, in the absence of significant plasticity, the J-integral parameter, J^{s}, can be correlated with the SIF using:

$$K_{I} = \sqrt{E' J^{S}} \quad (6)$$

where E′ = E is for plane stress condition and E′ = E/(1−ν^2) for plane strain condition [36]. According to the Paris law, under cyclic loading conditions the fatigue crack growth rate, da/dN, can be correlated with the SIF range using a power-law equation given by:

$$\frac{da}{dN} = C(\Delta K)^{n} \quad (7)$$

where C and n are material constants for a given value of stress ratio and temperature and can be obtained from a regression fit made to the da/dN versus ΔK data. To calculate the crack propagation life, the integrated form of the Paris equation can be used:

$$N_{p} = \int_{a_j}^{a_i} \frac{da}{C(\Delta K)^{n}} \quad (8)$$

where ai and aj are the initial crack length and propagated crack length, respectively, C and n are material constants, da/dN is the crack growth rate, and ΔK is the SIF range. The solution of the effective SIF range, ΔK_{eff}, can be obtained by:

$$\Delta K_{eff} = K_{\max} - K_{open} \quad (9)$$

where K_{max} is the SIF at the maximum load and K_{open} is the opening SIF to allow for crack closure. Under the thermal fatigue loading condition, k_{eff} describes the influence of oxidation, material degradation and plastic deformation at the vicinity of the crack [16]. The recognized relationships to describe the dependency of k_{eff} on the SIF range are:

$$\Delta K = f'(a') = f'(k_{eff} a) \quad (10)$$

$$\Delta K_{eq} = f(a) = f\left(\frac{a'}{k_{eff}}\right) \quad (11)$$

where $\Delta K = K_{max} - K_{min}$, and a and a′ are the tested and simulated crack length, respectively.

3.2. FINITE ELEMENT SIMULATIONS

To evaluate the thermal crack growth behaviour of the Ni75 alloy in the presence and absence of residual stresses, a complete coupled temperature-displacement FE model was developed. The ABAQUS standard solver was used for the FE simulations. Following the experimental thermal fatigue test procedure, the thermal stress field was calculated with the coupled temperature-displacement method. For this purpose, a centre hole edge cracked specimen with the same geometry as the thermal fatigue test specimens were modelled. The thermal loading and boundary conditions were identical to the thermal fatigue experiments. Each specimen sustained five thermal cycles and was subject to three thermal loading conditions during each cycle. Each thermal cycle included a transient temperature increase up from room temperature to 700 °C, a steady-state condition at the temperature of 700 °C, and a transient temperature decrease to room temperature (see **Figure 6**). The parameters needed were obtained by the material properties curves (**Figure 1**). The DLOAD subroutine was implemented in ABAQUS simulations to implement the residual stress field, which was previously obtained by the XRD technique, in the FE simulations [42]. In the FE model, a region with a depth of 0.5 mm was assigned an initial residual stress field according to XRD measurement data (**Figure 5**). To simplify the model and reduce the computational power time and power, it is fair to assume that (with a defined coordinate system):

$$\sigma_{11} = \sigma_{22} \quad (12)$$

$$\sigma_{33} = \sigma_{12} = \sigma_{13} = \sigma_{23} = 0 \quad (13)$$

Based on the results obtained from the thermal fatigue experiments, 7 different crack lengths (from 0.1 mm to 3 mm) for the NSP specimen and 7 different crack lengths (from 0.1 mm to 1.62 mm) for the SP specimen were used to calculate the maximum stress intensity factor at the crack tip and the J-integral at each condition. A coupled displacement-temperature 8-node quadratic tetrahedron elements with reduced integration (C3D8RT) were used to mesh the model. A mesh sensitivity analysis was carried out to find a suitable number of elements in the region of interest (i.e. crack path). Ultimately, the FE model was contented with a total number of 29712 elements and 40792 nodes. The local grid refinement was used to refine the mesh in the vicinity of the crack. The meshed model of the crack tip in the FE simulation is shown in **Figure 7(a)**. Full stress and strain analyses were carried out on the models. In order to verify the FE model, the experimental test results were compared with the crack propagation predicted by the ZENCRACK fracture mechanic code. ZENCRACK is an FE code that is developed for general 3D crack growth analysis and is used to calculate fracture mechanics parameters. ZENCRACK reads the ABAQUS data file for the un-cracked mesh and to generate a cracked mesh it is the replacement of one or more elements in an un-cracked mesh using crack-blocks. Two standard and large crack blocks can be used to create a 3D crack [43]. In this study, the standard crack block (s04_t35x1) was used to simulate the crack growth (**Figure 7(b)**). The specification of elements used for crack growth is summarised in **TABLE 2**.

Table 2. Specification of elements used for crack growth

Element name	Type	Total Elements
s04_t35x1	Through crack block (standard method)	4066

4. RESULTS AND DISCUSSIONS

4.1. CRACK GROWTH ANALYSIS

Based on the experimental testing procedure, two 3D FE models without (i.e. to replicate NSP specimens) and with residual stress (i.e. to replicate SP specimens) induced by the shot peening process were modelled in ABAQUS. Temperature distribution and the total normal stress distribution (i.e. along the Y direction) resulting from the transient thermal load at the maximum load condition are shown in **Figure 8**. The maximum recorded value of normal stress at the hole edge in the NSP specimen (without residual stress) and

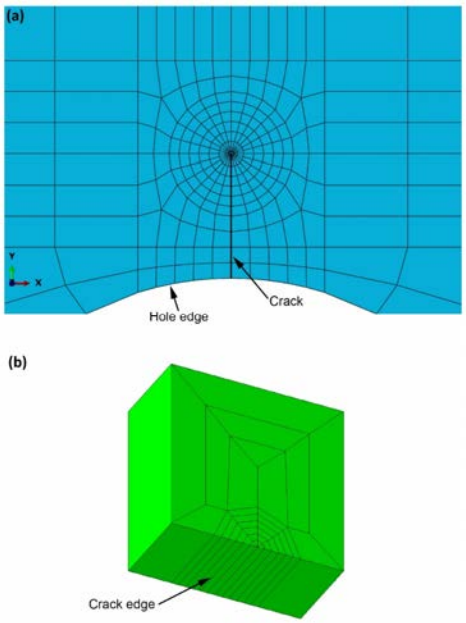


Figure 7. FE model (a) thermal fatigue specimen meshed geometry with a crack, and (b) the element s04_t35x1 schematic

in the SP specimen (with residual stress) are 823 and 537 MPa, respectively. The normal stress (i.e. along the Y direction) distribution resulting from the thermal loading on the crack growth route of the two specimens is shown in **Figure 9**. As seen in this figure, the maximum stress value at the zero distance from the hole edge is about 1.5 times more in the NSP specimen than the SP specimen. The experimental variations of thermal fatigue crack propagation for the two conditions are shown in **Figure 10**. The obtained crack propagation results for each condition (NSP and SP) are averaged from three repeated tests. It was experimentally observed that for each of the NSP and SP conditions the deviation of the results in the repeated tests was very minor; therefore, the averaged data are plotted here. The crack initiation life is defined as the number of thermal cycles when the thermal fatigue crack reaches 0.05 mm length. The Figure shows that the fatigue life has been significantly improved by compressive residual stress induced due to the shot peening process. In the developed crack growth prediction model, the experimental crack growth rates for the NSP and SP conditions were employed in the calculations; thus, the crack propagation rates were extracted from **Figure 10** by mathematical differentiation, and the crack propagation rate versus the crack length and the number of thermal cycles is plotted in **Figure 11(a)** and **(b)**, respectively. Based on the experimental thermal fatigue test results, 7 different crack lengths (from 0.1 mm to 3 mm) for the NSP specimen and 7 different crack lengths (from 0.1 mm to 1.62 mm) for the SP specimen were used to calculate K_{max} at the crack tip. The correlations of K_{max}

with the crack length and cycle time at the crack length of 1 mm are shown in **Figure 12** for the NSP and SP conditions. The propensities of K_{max} at the vicinity of crack versus crack length are vital in evaluating the crack growth behaviour. Based on the crack propagation rate curves (**Figure 11**), the da/dN data first increased by increasing the crack length, and then decreased for both NSP and SP conditions; therefore, the behaviour of K_{max} is comparable to the experimental crack propagation rates. Moreover, **Figure 12** showed an increase in K_{max} during the heating up step, which was approximately stabilized at the steady-state step, and then decreased during the cooling down step. To calculate the required parameters that were mentioned before in section 3.1 and were used in the model, a_{max} and a'_{max} must be defined; therefore, it could be approximately calculated that a'_{max} is equal to 3 mm (**Figure 12(a)**) and a_{max} can be approximated from **Figure 10** to be equal to 3 and 1.62 mm, for NSP and SP conditions, respectively. A model based on the Paris law, presented in section 3.1, was employed to calculate the thermal fatigue crack growth behaviour and fatigue life. To evaluate the thermal fatigue crack growth behaviour and life, it is required to determine the relationship between the thermal fatigue crack propagation rate and ΔK. The relationship between the thermal fatigue crack propagation rate and ΔK for the NSP and SP conditions are shown in **Figure 13** in logarithmic scale. It can be observed that ΔK_{eq} and da/dN are linearly related in logarithmic scale; therefore, the linear regression was carried out on the data to obtain a relationship between ΔK_{eq} and da/dN and then the Paris equation constants were obtained. The obtained parameters from the fitted line made to the data in **Figure 13** are presented in **TABLE 3.**

To calibrate the fitted parameters that were obtained from the model, and for comparison between the experimental data and numerical predictions, the ZENCRACK fracture mechanic code was used. The comparison between the FE model and experimental data are plotted in **Figure 14**. As seen in this figure, a good agreement can be observed between the simulated and experimental crack growth results, indicating that the model appropriately predicted the thermal fatigue life for both NSP and SP conditions. **Figure 15** shows the evaluated crack growth profiles via ZENCRACK at the different crack propagation stages. According to **Figure 15**, The crack propagated along the X direction from the hole edge. As can be observed in this figure, in the first stage of crack growth the crack propagated slowly, and the crack growth profiles were close to each other while in the second stage of crack growth, the crack propagated rapidly and the crack growth profiles were further apart from each other. Lastly, in the final stage of crack growth, the crack propagated steadily and the crack profiles were compressed leading to the crack eventually stop. The obtained experimental and FE model parameters and the ΔK_{eq} participate in the proposed model. Comparison of the experimental and simulated crack propagation rate, da/dN, versus both crack length and number of thermal cycles for NSP and SP conditions are plotted in **Figure 16**. As seen in this figure, a good agreement has been found between the simulation results and the experimental test data. Based on these results, the model can appropriately predict the thermal fatigue life of the material.

Table 3. The fitted lines parameters

Condition	NSP specimen	SP specimen
Fitted line equations	$y = 2.023x - 5.976$	$y = 6.363x - 11.879$
n	2.023	6.363
C	1.07×10^{-06}	1.35×10^{-12}

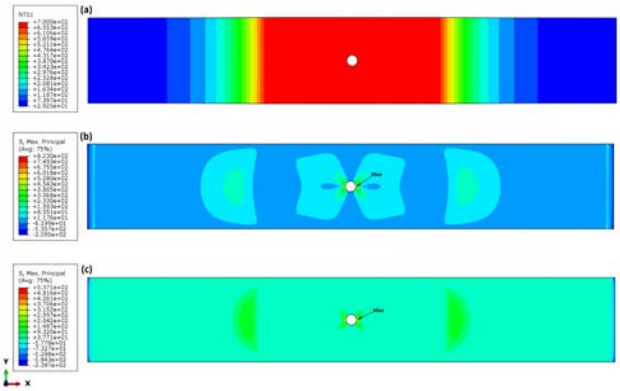


Figure 8. FE simulation results at the maximum load condition in MPa: (a) nodal temperature distribution; (b) normal stress (i.e. along the Y direction) of the NSP specimen; (c) normal stress (i.e. along the Y direction) of the SP specimen

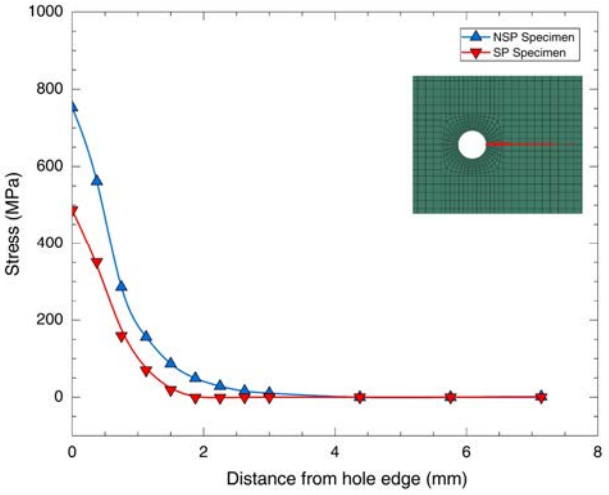


Figure 9. Normal stress (i.e. along the Y direction) distribution on the crack propagation path of two specimens

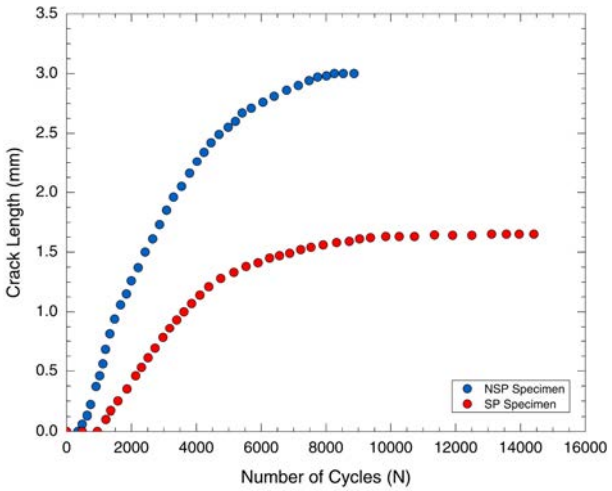


Figure 10. The thermal fatigue life curve for crack growth

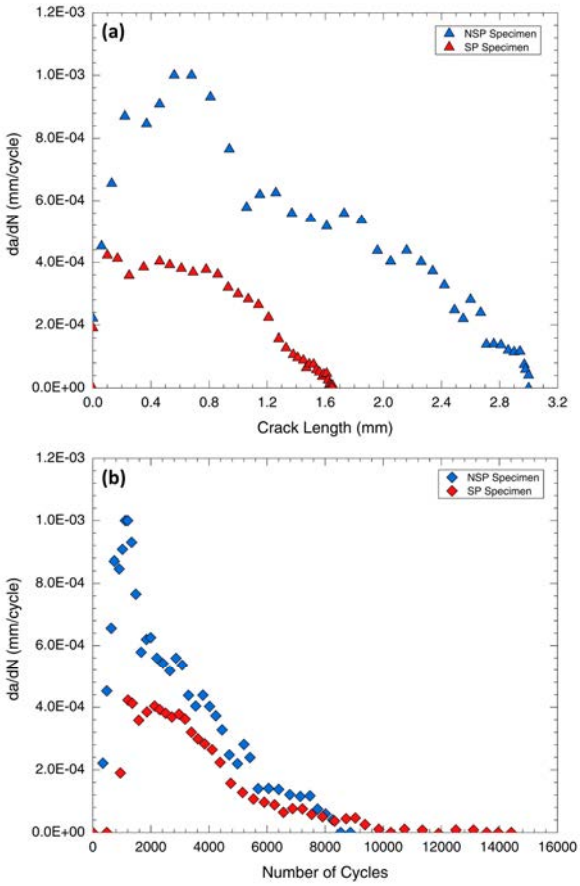


Figure 11. The crack propagation rates for the NSP and SP conditions against (a) the crack length, and (b) the number of cycles

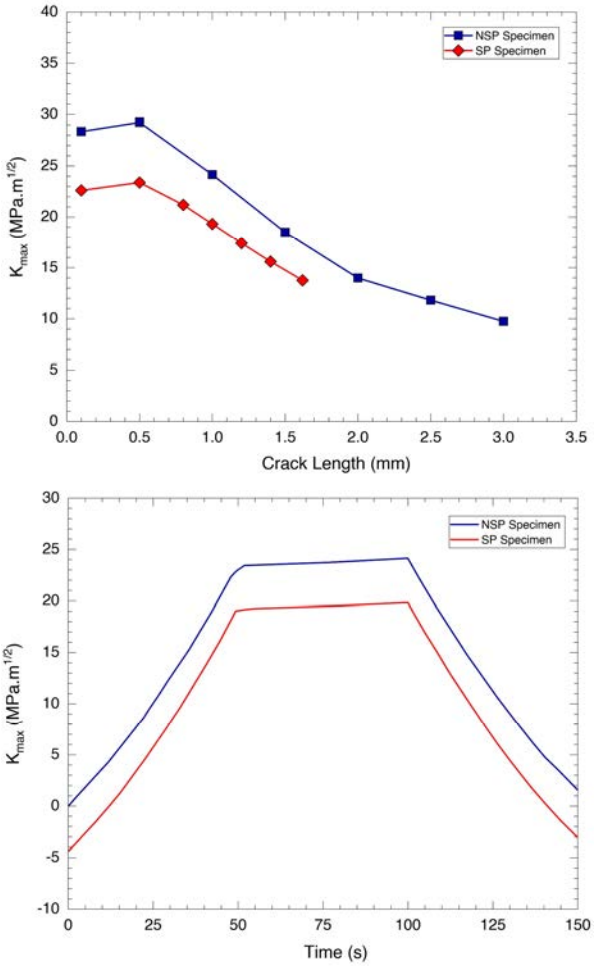


Figure 12. The simulated SIF for NSP and SP conditions against (a) the crack length, and (b) the cycle time at the crack length of 1 mm

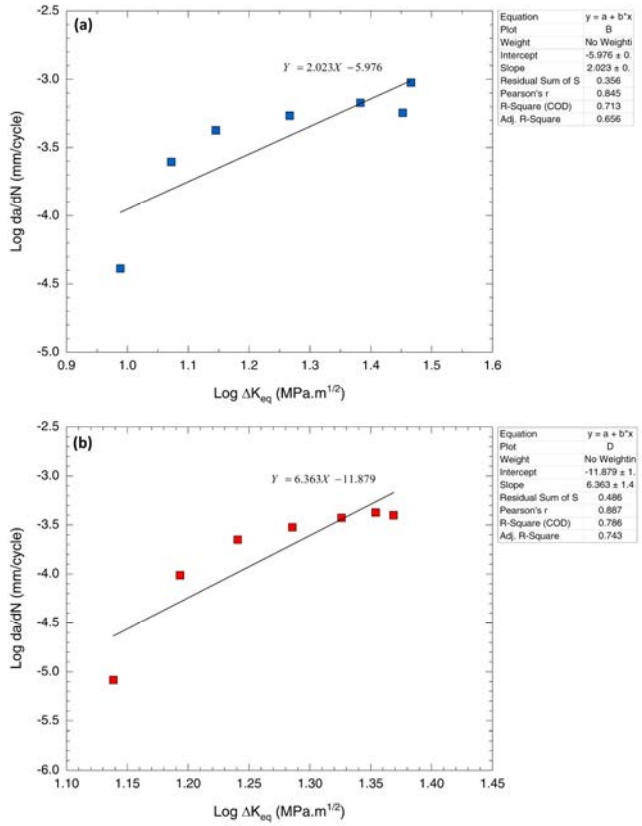


Figure 13. da/dN versus ΔK_{eq} in the logarithmic scale and the lines of best fit made to the data for: (a) NSP specimen, and (b) SP specimen

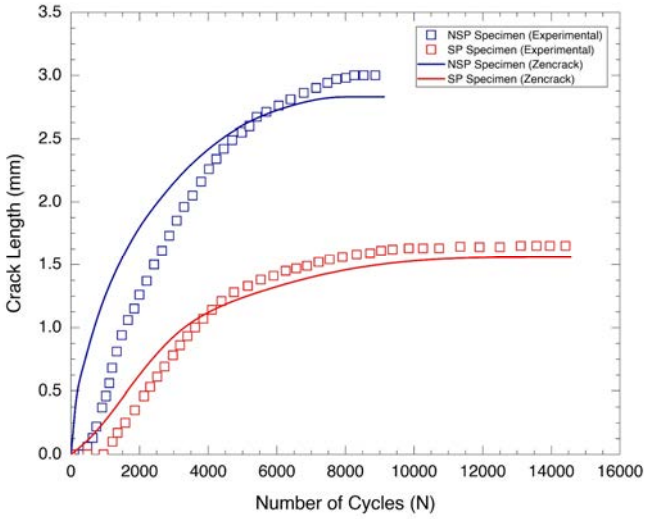


Figure 14. Comparison between experimental and FE crack growth results for NSP and SP conditions

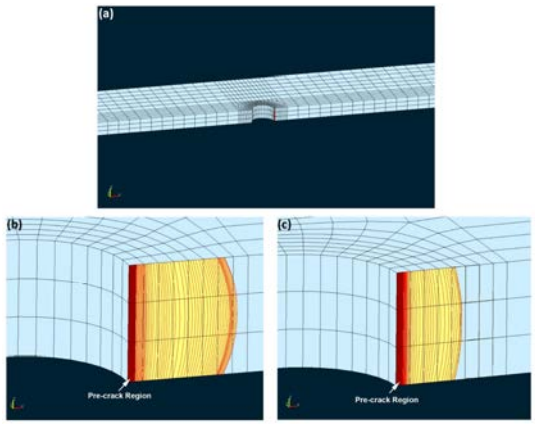


Figure 15. Simulated crack growth profiles: (a) specimen cut view, (b) NSP specimen, (c) SP specimen

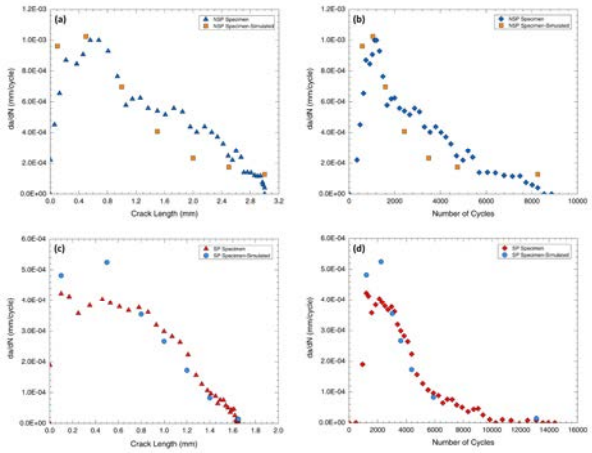


Figure 16. Comparison of the experimental and simulated crack propagation rates versus crack length and the number of thermal cycles for: (a and b) NSP condition, and (c and d) SP condition

4.2. MICROSCOPY ANALYSIS

To investigate and characterise the failure mechanisms, the fractured thermal fatigue test specimens were separately examined and analysed using optical microscopy (OM) and scanning electron microscopy (SEM) techniques. In order to perform the microscopy analysis, the specimens were prepared following the standard metallographic procedure and then etched by the solution of 45.4 gr of $FeCl_3$, 18 ml of HCl, 15 ml of H_2SO_4, 50 ml of HNO_3, 75 ml of $C_2H_4O_2$, and 75 ml of distilled water. Thermal fatigue crack propagation routes were determined on the side faces of the specimens. Optical micrographs of the two test conditions (without and with residual stress) are shown in **Figure 17**. It can be observed in this figure that at the crack origin (notch) and near the crack tip region, the distance between the crack flanks of the SP specimen is about 1.4 times smaller than the NSP specimen. This observation shows that the induced residual stress in the SP specimen reduced the crack opening.

Furthermore, there was no evidence of plastic deformation due to crack closure observed in the crack flanks. Following the OM analysis, SEM analysis was conducted on the thermal fatigue specimens as shown in **Figure 18**. This figure demonstrates the thermal fatigue cracking mode at the hole edge region where the crack initiates, the crack route, and the crack tip of the NSP and SP specimens. As seen in **Figure 18**, secondary cracks and crack branching are visible and shown by yellow arrows for both NSP and SP conditions. At the hole edge region, some secondary cracks are visible near the main crack that is propagated from the notched edge. Also, at the crack route region, the NSP specimen has more secondary cracks and crack branching than the SP specimen, and at the crack tip region crack branching in the NSP specimen is much more than the SP specimen. Moreover, the secondary cracks in the NSP specimen are longer than the SP specimen. Therefore, the results show that smaller distances between crack flanks, secondary cracks, as well as crack branching, are the result of the residual stresses induced by the shot peening process. The detailed SEM micrographs of the thermal fatigue crack tip for the NSP and SP specimens are shown in **Figure 19**. As seen in **Figure 19**, in the NSP specimen the crack was propagated into the grain and the trans-granular cracking mode can be observed. In the SP specimen, a combination of inter and trans-granular crack growth with trans-granular crack branching can be observed. Also seen in this figure is that the thermal fatigue crack rapidly shifted between inter-granular and trans-granular cracking during the propagation. Finally seen in both NSP and SP conditions is that the carbides precipitated in the grain boundaries and matrix. Following the SEM analysis, the Energy Dispersive X-Ray (EDS) analysis was conducted on the test specimens and the results are shown in **Figure 20**. As seen in this figure, three EDS points were taken from the matrix, crack opening mouth, and carbide, respectively. It can be observed in **Figure 20** that Ni and Fe were segregated mainly into the matrix, and Cr and C were generally found in carbides. Furthermore, some elements, such as Oxygen, were observed in the crack mouth of both NSP and SP specimens, resulting from the corrosion process. Due to the high-temperature cyclic process, Oxygen is generally found in the crack mouth in the thermal fatigue fracture mechanism. **Figure 21** shows the features of the fractured surface and crack initiation points of the NSP and SP specimens. The figure shows the fractured surface and cracks propagation region from the hole edge. As seen in this figure, thermal fatigue cracks of the NSP and SP specimens are initiated from the hole edge (shown with yellow arrows). The thermal fatigue crack origin of the NSP and SP specimens is in-depth of 200 and 510 μm from the surface of specimens, respectively. Thus, in the NSP specimen, the thermal fatigue crack initiated near the surface of the specimen, and in the SP specimen, the subsurface cracking occurred far from the surface of the specimen. Also, the first traces of plastic deformation were visible nearly instantly in the vicinity of the hole edge, and the microcrack initiation occurred after the first few cycles. Consequently, the residual stresses induced by the shot peening process prevented cracking near the surface of the specimen, where the magnitude of compressive stress is high. The fatigue features in fractured NSP and SP test specimens are shown in **Figure 22**. As seen in this figure, the fatigue striations (shown with yellow arrows) appeared on the fractured surface of both NSP and SP specimens. The striations were uniform at both specimens. Furthermore, the microcracks (shown with blue arrows), and in the thermal fatigue crack propagation region some oxidation features and small cavities (shown with green arrows) were observed. It can be observed in **Figure 22** that microcracks in the NSP specimen are more than the SP specimen. Furthermore, some presence of tear ridge (shown with red arrows) were seen in the fracture region of the SP specimen. This indicates that the fracture was occurred by plastic collapse since the Ni75 alloy matrix is ductile and the carbides are hard; thus, the matrix was plastically deformed around the carbides.

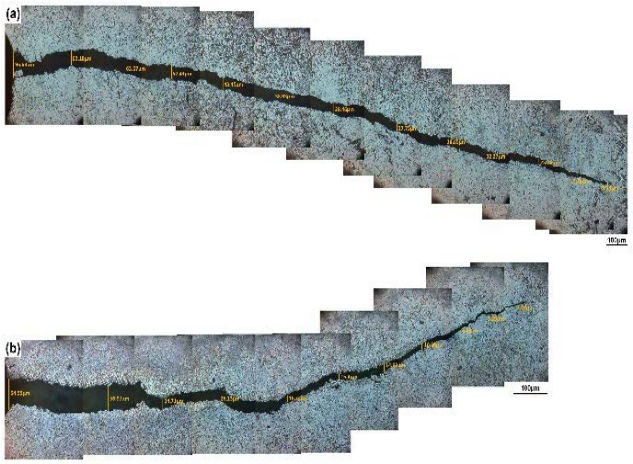


Figure 17. Optical micrographs of the thermal fatigue crack: (a) NSP specimen, and (b) SP specimen

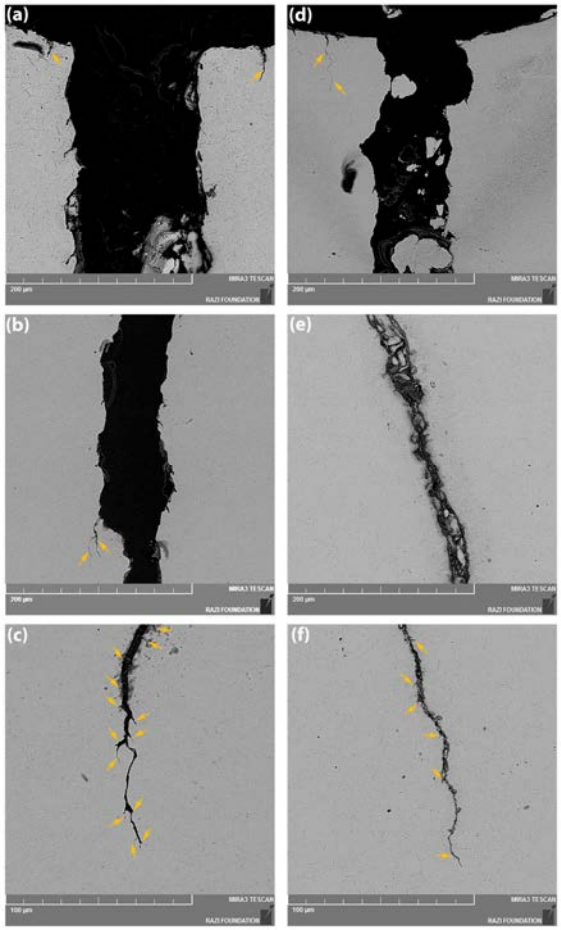


Figure 18. SEM micrographs of the thermal fatigue cracks: (a, b and c) NSP specimen, and (d, e and f) SP specimen

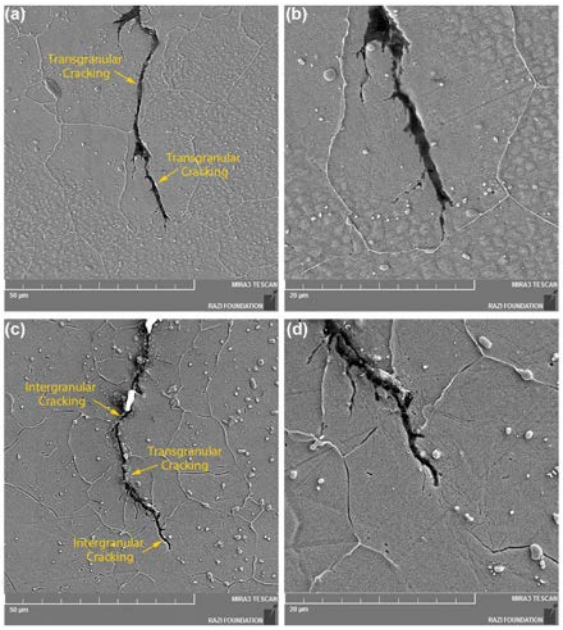


Figure 19. SEM micrographs of the thermal fatigue crack tip: (a and b) NSP specimen, (c and d) SP specimen

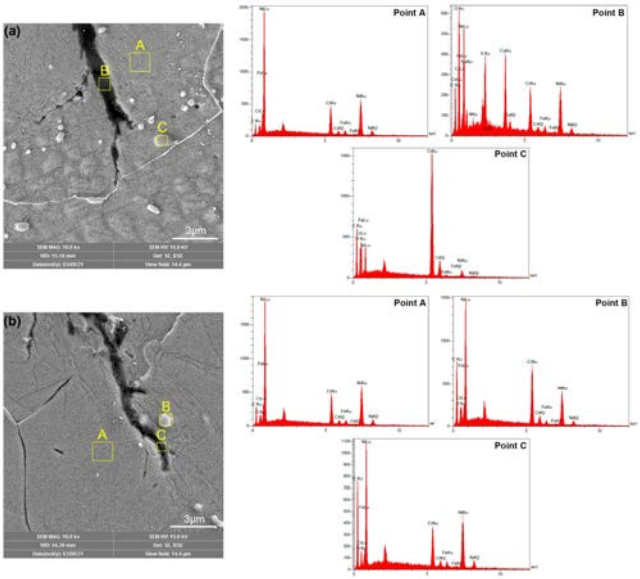


Figure 20. EDS point analysis; (a) NSP specimen, and (b) SP specimen

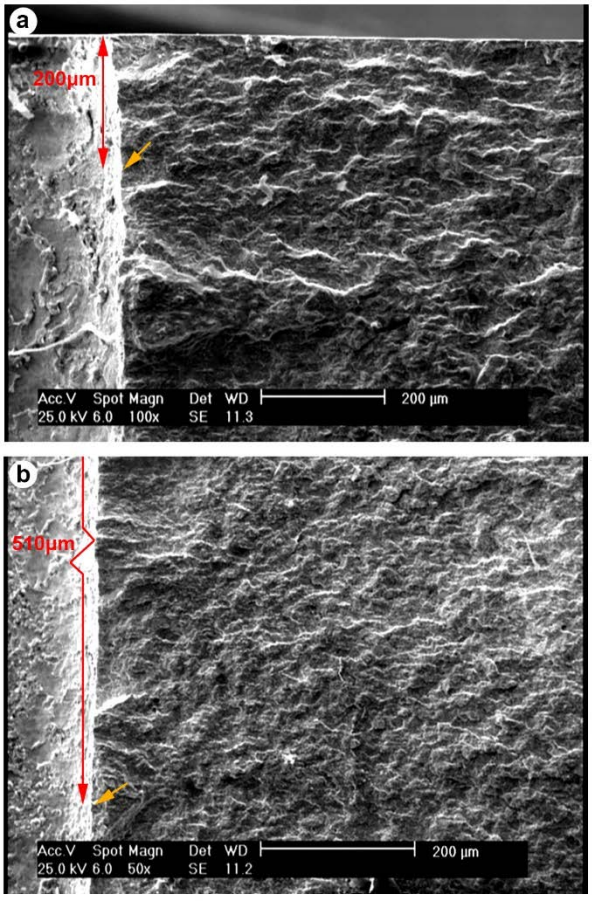


Figure 21. The fractured surface of the test specimens: (a) NSP condition, (b) SP condition

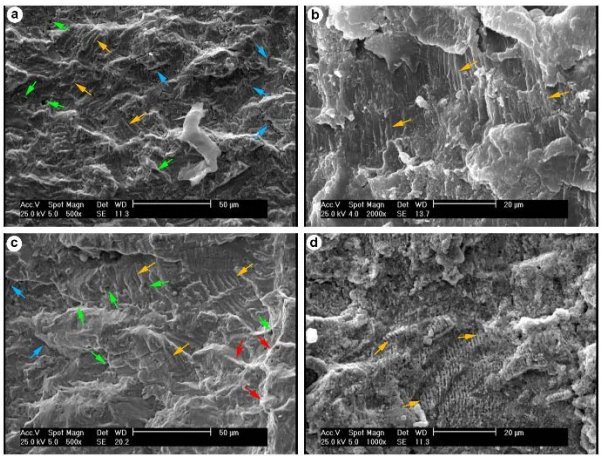


Figure 22. SEM images of the fatigue fracture features and the morphology of striations: (a and b) NSP specimen, and (c and d) SP specimen

5. CONCLUSION

In this study, experimental tests and FE analyses were carried out to propose a model for predicting the thermal fatigue crack propagation behaviour of the shot peened Ni75 alloy. Based on the obtained results, the following conclusions were drawn:

1. The FE simulation showed that the stress distribution on the NSP specimen was more concentrated than the SP specimen. Also, the compressive residual stress induced by the shot peening process reduced the stress distribution along the crack propagation path. Therefore, based on FE analysis, the residual stress induced by the shot peening process reduced the thermal stress values, especially in the critical points for thermal fatigue crack initiation.
2. Based on experimental thermal fatigue tests, the crack initiation life of the SP specimen is about 2.5 times more than the NSP specimen.
3. The simulated K analysis showed an increase during the heating up stage, almost stabilized at the steady-state stage, and then decreased during the cooling down process; thus, the thermal fatigue crack was propagated during heating up.
4. The ZENCRACK fatigue life prediction results based on the Paris equation constants obtained from the proposed model showed good agreement between the numerical and experimental results.
5. The comparison between experimental and simulated results showed that the proposed approach can appropriately predict the thermal fatigue crack growth behaviour of both NSP and SP conditions by using a combination of FE simulation and experimental test data.
6. Optical micrographs showed that the distance between the crack flanks in the SP specimen is smaller than the NSP specimen. This shows that the induced residual stress in the SP specimen reduced the crack opening.
7. The SEM micrographs from the thermal fatigue crack path showed that the shot peening process affected the thermal fatigue crack initiation and propagation. Smaller distances between crack flanks, secondary cracks, as well as crack branching, are the results of residual stresses induced by the shot peening process.
8. The failure mechanism of the NSP condition was found to be trans-granular and the SP condition was a combination of inter and trans-granular cracking.

6. ACKNOWLEDGMENT

The corresponding author would like to acknowledge Dr. H. Hassani Najafabdi from Politecnico di Torino for providing help that greatly assisted the conduction of this research. Also, that the assistance of Ms. Z. Khoshkhou-Gilavaei from the University of Tehran for editorial contribution is gratefully acknowledged.

7. CONFLICTS OF INTEREST

The authors declare that they have no known competing financial interests or personal relationships that could have appeared to influence the work reported in this paper.

REFERENCES

1. J. Zhang, Z. Zhao, Y. Kong, Z. Zhang, Q. Zhong, Crack initiation and propagation mechanisms during thermal fatigue in directionally solidified superalloy DZ125, International Journal of Fatigue 119 (2019) 355-366
2. T. Goswami, Low cycle fatigue—dwell effects and damage mechanisms, International Journal of Fatigue 21(1) (1999) 55-76.https://doi.org/10.1016/S0142-1123(98)00056-5
3. B. Salehnasab, E. Poursaeidi, S.A. Mortazavi, G.H. Farokhian, Hot corrosion failure in the first stage nozzle of a gas turbine engine, Engineering Failure Analysis 60 (2016) 316-325.https://doi.org/10.1016/j.engfailanal.2015.11.057
4. B. Salehnasab, J. Marzbanrad, E. Poursaeidi, Transient thermal fatigue crack propagation prediction in a gas turbine component, Engineering Failure Analysis 130 (2021)

105781.https://doi.org/10.1016/j.engfailanal.2021.105781
5. K. Kikuchi, K. Ue, Y. Kudo, M. Saito, Crack propagation in first wall by thermal fatigue and creep, Fusion Engineering and Design 49-50 (2000) 229-234.https://doi.org/10.1016/S0920-3796(00)00363-X
6. J. Yang, Q. Zheng, X. Sun, H. Guan, Z. Hu, Thermal fatigue behavior of K465 superalloy, Rare Metals 25(3) (2006) 202-209.https://doi.org/10.1016/S1001-0521(06)60040-5
7. F. Meyer-Olbersleben, N. Kasik, B. Ilschner, F. Rézaï-Aria, The thermal fatigue behavior of the combustor alloys In 617 and HAYNES 230 before and after welding, Metallurgical and Materials Transactions A 30(4) (1999) 981-989.10.1007/s11661-999-0151-4
8. E. Poursaeidi, H. Bazvandi, Effects of emergency and fired shut down on transient thermal fatigue life of a gas turbine casing, Applied Thermal Engineering 100 (2016) 453-461.https://doi.org/10.1016/j.applthermaleng.2016.02.049
9. E. Poursaeidi, A. Kavandi, K. Vaezi, M.R. Kalbasi, M.R. Mohammadi Arhani, Fatigue crack growth prediction in a gas turbine casing, Engineering Failure Analysis 44 (2014) 371-381.https://doi.org/10.1016/j.engfailanal.2014.05.010
10. E.k. Yousefabad, S. Asadi, P. Savadkouhi, O. Sedaghat, A. Bakhshi, The effect of non-uniform combustion temperature profile on thermal fatigue cracking of an air-cooled gas turbine vane, Engineering Failure Analysis 105 (2019) 766-780.https://doi.org/10.1016/j.engfailanal.2019.07.008
11. D. Bombač, M. Gintalas, G. Kugler, M. Terčelj, Thermal fatigue behaviour of Fe-1.7C-11.3Cr-1.9Ni-1.2Mo roller steel in temperature range 500–700 °C, International Journal of Fatigue 121 (2019) 98-111.https://doi.org/10.1016/j.ijfatigue.2018.12.007
12. Z.Z. Li WANG, Shaohua ZHANG,Xiangdong JIANG,Langhong LOU,Jian ZHANG, Crack initiation and propagation around holes of Ni-based single crystal superalloy during thermal fatigue cycle, Acta Metall Sin 51(10) (2015) 1273-1278.10.11900/0412.1961.2015.00366
13. R. Vetriselvan, P. Sathiya, G. Ravichandran, Experimental and numerical investigation on thermal fatigue behaviour of 9Cr 1Mo steel tubes, Engineering Failure Analysis 84 (2018) 139-150.https://doi.org/10.1016/j.engfailanal.2017.11.005
14. B. Liu, B. Wang, X. Yang, X. Zhao, M. Qin, J. Gu, Thermal fatigue evaluation of AISI H13 steels surface modified by gas nitriding with pre- and post-shot peening, Applied Surface Science 483 (2019) 45-51.https://doi.org/10.1016/j.apsusc.2019.03.291
15. F. Qayyum, M. Shah, O. Shakeel, F. Mukhtar, M. Salem, F. Rezai-Aria, Numerical simulation of thermal fatigue behavior in a cracked disc of AISI H-11 tool steel, Engineering Failure Analysis 62 (2016) 242-253.https://doi.org/10.1016/j.engfailanal.2016.01.015
16. H. Pei, Z. Wen, Z. Wang, W. Gan, G.X. Lu, Z. Yue, Transient thermal fatigue crack propagation behavior of a nickel-based single-crystal superalloy, International Journal of Fatigue 131 (2020) 105303.https://doi.org/10.1016/j.ijfatigue.2019.105303
17. H. Pei, Y. Zhang, Z. Wen, J. Wang, X. Ai, Z. Yue, Crack initiation behavior of a Ni-based SX superalloy under transient thermal stress, Materials Science and Engineering: A 754 (2019) 581-592.https://doi.org/10.1016/j.msea.2019.03.112
18. H. Bazvandi, E. Poursaeidi, Effect of additional holes on crack propagation and arrest in gas turbine casing, Engineering Failure Analysis 111 (2020) 104443.https://doi.org/10.1016/j.engfailanal.2020.104443
19. M. Banaszkiewicz, Numerical investigations of crack initiation in impulse steam turbine rotors subject to thermo-mechanical fatigue, Applied Thermal Engineering 138 (2018) 761-773.https://doi.org/10.1016/j.applthermaleng.2018.04.099
20. L.B. Getsov, A.S. Semenov, I.A. Ignatovich, Thermal fatigue analysis of turbine discs on the base of deformation criterion, International Journal of Fatigue 97 (2017) 88-97.https://doi.org/10.1016/j.ijfatigue.2016.12.018
21. S. Mazlan, N. Yidris, S.S. Koloor, M. Petrů, Experimental and Numerical Analysis of Fatigue Life of Aluminum Al 2024-T351 at Elevated Temperature, Metals, 2020.
22. Z. Qin, B. Li, H. Zhang, T.Y.A. Wilfried, T. Gao, H. Xue, Effects of shot peening with different coverage on surface integrity and fatigue crack growth properties of 7B50-T7751 aluminum alloy, Engineering Failure Analysis 133 (2022) 106010
23. C. Wang, G. Wu, T. He, Y. Zhou, Z. Zhou, Numerical Study of Fatigue Crack Propagation in a Residual Stress Field Induced by Shot Peening, Journal of Materials Engineering and

Performance 29(8) (2020) 5525-5539.10.1007/s11665-020-05029-9
24. Y. Wang, Y. Zhang, G. Song, W. Niu, Z. Xu, C. Huang, Effect of shot peening on fatigue crack propagation of Ti6Al4V, Materials Today Communications 25 (2020) 101430.https://doi.org/10.1016/j.mtcomm.2020.101430
25. B.Y. He, K.A. Soady, B.G. Mellor, G. Harrison, P.A.S. Reed, Fatigue crack growth behaviour in the LCF regime in a shot peened steam turbine blade material, International Journal of Fatigue 82 (2016) 280-291.https://doi.org/10.1016/j.ijfatigue.2015.03.017
26. N. Ferreira, P.V. Antunes, J.A.M. Ferreira, J. D. M. Costa, C. Capela, Effects of Shot-Peening and Stress Ratio on the Fatigue Crack Propagation of AL 7475-T7351 Specimens, Applied Sciences, 2018.
27. S. Li, W. Liang, H. Yan, Y. Wang, C. Gu, Prediction of fatigue crack propagation behavior of AA2524 after laser shot peening, Engineering Fracture Mechanics 268 (2022) 108477.https://doi.org/10.1016/j.engfracmech.2022.108477
28. F. Szmytka, M. Salem, F. Rézaï-Aria, A. Oudin, Thermal fatigue analysis of automotive Diesel piston: Experimental procedure and numerical protocol, International Journal of Fatigue 73 (2015) 48-57.https://doi.org/10.1016/j.ijfatigue.2014.11.011
29. D. Klobčar, L. Kosec, B. Kosec, J. Tušek, Thermo fatigue cracking of die casting dies, Engineering Failure Analysis 20 (2012) 43-53.https://doi.org/10.1016/j.engfailanal.2011.10.005
30. D. Mellouli, N. Haddar, A. Köster, A.M.-L. Toure, Thermal fatigue of cast irons for automotive application, Materials & Design 32(3) (2011) 1508-1514.https://doi.org/10.1016/j.matdes.2010.10.025
31. M. Fazarinc, T. Muhič, G. Kugler, M. Terčelj, Thermal fatigue properties of differently constructed functionally graded materials aimed for refurbishing of pressure-die-casting dies, Engineering Failure Analysis 25 (2012) 238-249.https://doi.org/10.1016/j.engfailanal.2012.05.016
32. H.-W. Song, G. Yu, J.-S. Tan, L. Zhou, X.-L. Yu, Thermal fatigue on pistons induced by shaped high power laser. Part I: Experimental study of transient temperature field and temperature oscillation, International Journal of Heat and Mass Transfer 51(3) (2008) 757-767.https://doi.org/10.1016/j.ijheatmasstransfer.2007.04.035
33. D. Cong, H. Zhou, Z. Ren, H. Zhang, L. Ren, C. Meng, C. Wang, Thermal fatigue resistance of hot work die steel repaired by partial laser surface remelting and alloying process, Optics and Lasers in Engineering 54 (2014) 55-61.https://doi.org/10.1016/j.optlaseng.2013.09.012
34. V.S. Bhattachar, Thermal fatigue behaviour of nickel-base superailoy 263 sheets, International Journal of Fatigue 17(6) (1995) 407-413.https://doi.org/10.1016/0142-1123(95)00006-F
35. X. Luo, N. Dang, X. Wang, The effect of laser shock peening, shot peening and their combination on the microstructure and fatigue properties of Ti-6Al-4V titanium alloy, International Journal of Fatigue 153 (2021) 106465.https://doi.org/10.1016/j.ijfatigue.2021.106465
36. G. Khajuria, M.F. Wani, High-temperature friction and wear studies of Nimonic 80A and Nimonic 90 against Nimonic 75 under dry sliding conditions, Tribology Letters 65(3) (2017) 100.10.1007/s11249-017-0881-1
37. Special Metals Standard, Ni 75 Alloy, Special Metals Corporation, USA.
38. S. International, Shot Peening AMS2430S, SAE, 2012.
39. B. Salehnasab, E. Poursaeidi, Mechanism and modeling of fatigue crack initiation and propagation in the directionally solidified CM186 LC blade of a gas turbine engine, Engineering Fracture Mechanics 225 (2020) 106842.https://doi.org/10.1016/j.engfracmech.2019.106842
40. X.-K. Zhu, Numerical Calculation of Residual Stress Corrected J-Integral Using ABAQUS, ASME 2014 33rd International Conference on Ocean, Offshore and Arctic Engineering, 2014.
41. Y. Lei, N.P. O'Dowd, G.A. Webster, Fracture mechanics analysis of a crack in a residual stress field, International Journal of Fracture 106(3) (2000) 195-216.10.1023/A:1026574400858
42. E. Maleki, G.H. Farrahi, K. Reza Kashyzadeh, O. Unal, M. Gugaliano, S. Bagherifard, Effects of Conventional and Severe Shot Peening on Residual Stress and Fatigue Strength of Steel AISI 1060 and Residual Stress Relaxation Due to Fatigue Loading: Experimental and Numerical Simulation, Metals and Materials International (2020).10.1007/s12540-020-00890-8
43. ZENCRACK User Manual, ZENTECH2019.